Insights Into the Electric Double-Layer Capacitance of the Two-Dimensional Electrically Conductive Metal-Organic Framework $Cu_3(HHTP)_2$

Jamie W. Gittins[1], Chloe J. Balhatchet[1], Yuan Chen[1, 2, 3], Cheng Liu[4], David G. Madden[5], Sylvia Britto[6], Matthias J. Golomb[7], Aron Walsh[7], David Fairen-Jimenez[5], Siân E. Dutton[4], Alexander C. Forse[1]*

[1] Yusuf Hamied Department of Chemistry, University of Cambridge, Lensfield Road, Cambridge CB2 1EW, U.K.

[2] Department of Chemistry, Imperial College London, Exhibition Road, London SW7 2AZ, U.K.

[3] The Faraday Institution, Quad One, Harwell Science and Innovation Campus, Didcot OX11 0RA, U.K.

[4] Cavendish Laboratory, University of Cambridge, JJ Thomson Avenue, Cambridge CB3 0HE, U.K.

[5] Adsorption & Advanced Materials Laboratory (A^2ML), Department of Chemical Engineering & Biotechnology, University of Cambridge, Philippa Fawcett Drive, Cambridge CB3 0AS, U.K.

[6] Diamond Light Source, Harwell Science and Innovation Campus, Didcot OX11 0DE, U.K.

[7] Department of Materials, Imperial College London, Exhibition Road, London SW7 2AZ, U.K.

ABSTRACT: Two-dimensional electrically conductive metal-organic frameworks (MOFs) have emerged as promising model electrodes for use in electric double-layer capacitors (EDLC). Here, we demonstrate the high capacitive performance of the framework $Cu_3(HHTP)_2$ (HHTP = 2,3,6,7,10,11-hexahydroxytriphenylene) with an organic electrolyte and compare its behaviour with the previously reported analogue, $Ni_3(HITP)_2$ (HITP = 2,3,6,7,10,11-hexaiminotriphenylene). At low current densities of 0.04 – 0.05 A g^{-1}, $Cu_3(HHTP)_2$ electrodes exhibit a specific capacitance of 110 – 114 F g^{-1} and show modest capacitance retentions (66 %) at current densities up to 2 A g^{-1}, mirroring the performance of $Ni_3(HITP)_2$ and suggesting that capacitive performance is largely independent of the identity of the metal node and organic linker molecule. However, we find a limited cell voltage window of 1.3 V and only moderate capacitance retention (86 %) over 30,000 cycles at a moderate current density of 1 A g^{-1}, both significantly lower than state-of-the-art porous carbons. These important insights will aid the design of future conductive MOFs with improved performance in EDLCs.

Introduction

The improvement of energy storage devices is critical for society to meet increasing energy demands and allow for the integration of renewable energy sources into energy grids[1–3]. Electric double-layer capacitors (EDLCs), a sub-set of supercapacitors, are among the most promising energy storage devices due to their high power densities, which result in rapid charging/discharging times, and excellent cyclability. As a result, EDLCs have potential uses in applications where other energy storage devices are not suitable e.g., in heavy electrical vehicles, storing energy rapidly from intermittent renewable energy sources[3–6]. However, state-of-the-art industrial EDLCs have low energy densities, which impedes their widespread use. Potential performance gains could be achieved by optimizing the structure of the electrodes and this may facilitate the use of supercapacitors more widely. Structure-property investigations to determine how performance varies with electrode structure are challenging with traditional EDLCs as many use porous carbons as the electrode material[7,8]. These tend to have poorly defined structures that are difficult to characterize, leading to structure-property investigations with conflicting results[9–14].

Recently, significant work has been done to develop new electrode materials for EDLCs with well-defined structures. One such class of materials is two-dimensional electrically conductive metal-organic frameworks (MOFs)[15]. These materials are generally formed from the square planar coordination of late transition metal M^{2+} nodes by planar conjugated organic linker molecules to form π-d conjugated 2D sheets. These sheets then stack, normally in an eclipsed or near-eclipsed fashion, to form an extended 3D honeycomb structure, creating pores that run through the material (**Fig. 1a**)[16,17]. Conductive MOFs are promising for use as EDLC electrodes as they have high intrinsic conductivities (up to 2500 S cm^{-1}) and porosities (surface

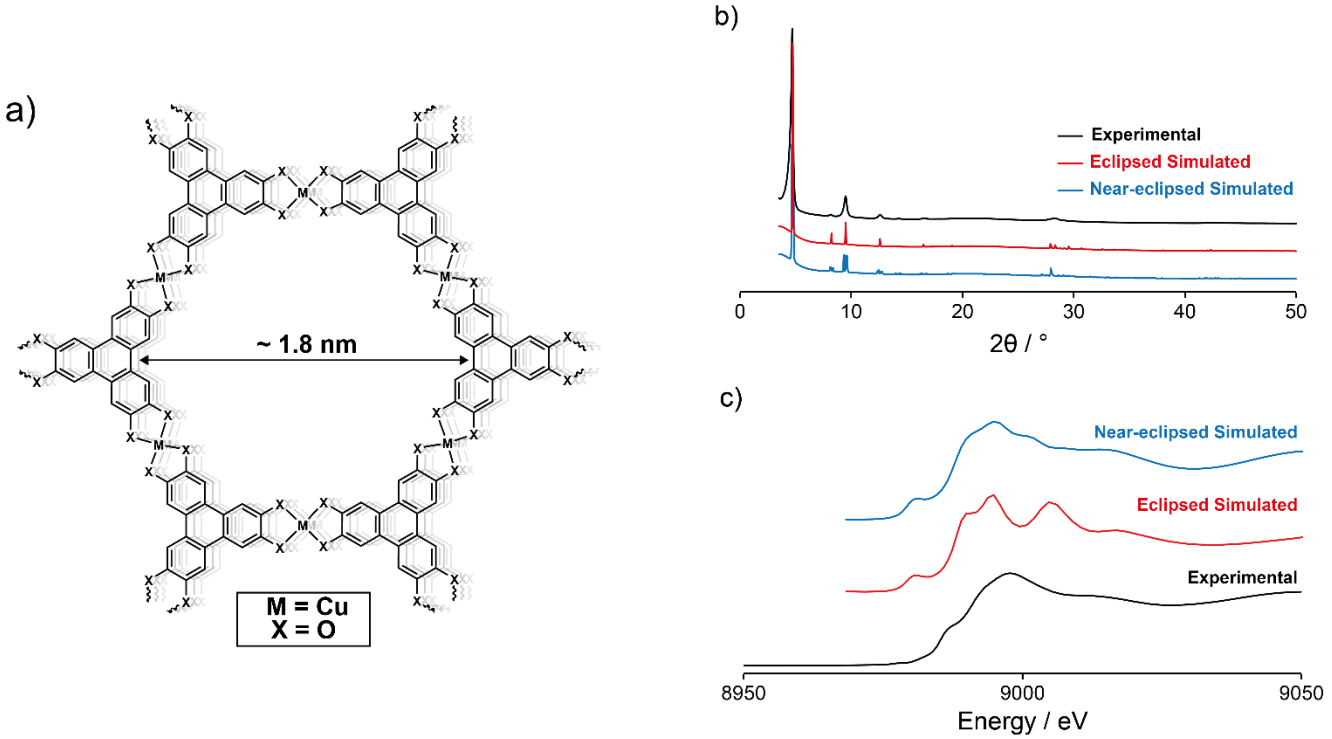

Figure 1: a) Schematic demonstrating the general structure of hexasubstituted triphenylene-based conductive MOFs. The π-d conjugated 2D sheets stack to form an extended 3D honeycomb structure. This creates pores/channels that run through the material, with a pore size of 1.8 nm as calculated from the simulated structure of $Cu_3(HHTP)_2$. b) The experimental PXRD pattern of $Cu_3(HHTP)_2$ compares well to simulated PXRD patterns of $Cu_3(HHTP)_2$ with both eclipsed and near-eclipsed crystal structure. c) Experimentally obtained Cu K-edge XANES of $Cu_3(HHTP)_2$ shows better agreement with the simulated XANES of $Cu_3(HHTP)_2$ with a near-eclipsed crystal structure.

areas of 500 – ca. 1400 $m^2\ g^{-1}$)[18–20]. Furthermore, the tunable crystalline structures of conductive MOFs make them interesting materials for use as model electrodes in structure-property investigations. Despite this promise and much exploration as electrode materials in other energy storage devices, including batteries, few conductive MOFs have been explored in EDLCs, particularly with more commercially relevant organic electrolytes[21–26]. However, a key example is $Ni_3(HITP)_2$ (HITP = 2,3,6,7,10,11-hexaiminotriphenylene), which demonstrated high capacitive behaviour (111 – 116 F g^{-1} at 0.05 A g^{-1}) as the sole electrode material in a symmetric EDLC with 1 M NEt_4BF_4 in acetonitrile electrolyte[27]. The closely related framework $Cu_3(HHTP)_2$ (HHTP = 2,3,6,7,10,11-hexahydroxytriphenylene) was also explored in EDLCs with aqueous and solid-state gel electrolytes, and while nanowire arrays (NWAs) of this MOF exhibited good capacitive performance, electrodes made using $Cu_3(HHTP)_2$ powder exhibited relatively poor capacitive behaviour[28,29]. Here we build on these studies and present a detailed analysis of the electric double-layer capacitance of $Cu_3(HHTP)_2$ in EDLCs with an organic electrolyte. Using a recently published synthesis, as well as traditional electrode film processing methods, we find that $Cu_3(HHTP)_2$ exhibits very similar performance to $Ni_3(HITP)_2$ in terms of capacitance, rate capability, and cycling stability, suggesting that EDLC performance is independent of the identity of the metal node and organic linker in these almost isostructural frameworks[30].

Results & Discussion

$Cu_3(HHTP)_2$ was synthesized by modifying a recently published procedure (see SI Methods)[30]. The identity and structure of the MOF were confirmed via powder X-ray diffraction (PXRD), with the experimentally obtained PXRD pattern comparing well to those simulated using hexagonal eclipsed and monoclinic near-eclipsed crystal structures of $Cu_3(HHTP)_2$, both polytypes of the C-centered monoclinic structure due to the sub-supergroup relation but with variations in the stacking of the 2D layers (**Fig. 1a, b**; SI Figs. S1, S2; Table S1). However, the quality of the PXRD data is insufficient for Rietveld refinement and therefore insufficient to distinguish between the models with any degree of certainty. To gain further information on the structure of the synthesized $Cu_3(HHTP)_2$, Cu K-edge X-ray absorption near edge structure (XANES) was performed on a powdered sample, and the obtained spectrum compared to those simulated using the two crystal structures described above (**Fig. 1c**). The results are supportive of previous work indicating that $Cu_3(HHTP)_2$ may have a near-eclipsed crystal structure, with a constant stacking shift of the 2D layers, as opposed to the closely related eclipsed structure exhibited by $Ni_3(HITP)_2$[31]. Cu K-edge XANES was also used to probe the Cu oxidation states present in the MOF. This confirmed that Cu(II) is the dominant Cu oxidation state in the as-synthesized MOF with no clear evidence for the presence of Cu(I) (SI Fig. S3). This result

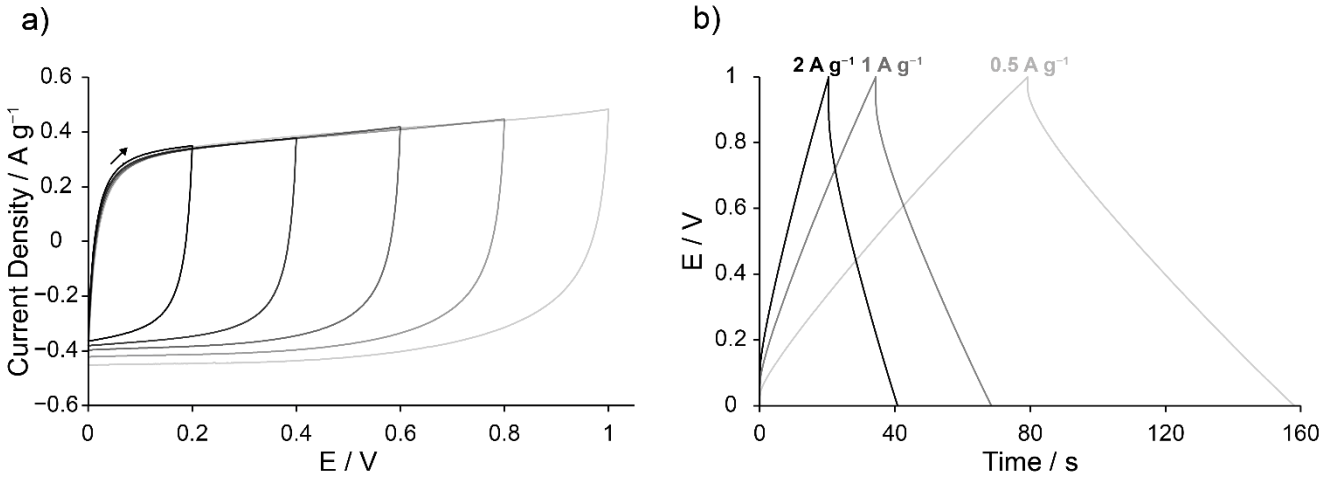

Figure 2: a) Cyclic voltammograms (CVs) at a scan rate of 10 mV s^{-1} up to 1.0 V show that $Cu_3(HHTP)_2$ displays predominantly double-layer capacitive behaviour in this voltage window in symmetric EDLCs with 1 M NEt_4BF_4 in acetonitrile electrolyte. The black arrow shows the direction of scanning from the start of the scan. b) Galvanostatic charge-discharge (GCD) profiles at a variety of current densities confirm this behaviour (see labels).

helps to clarify debate in the literature on the Cu oxidation states in the framework, with some previous XANES and X-ray photoelectron spectroscopy (XPS) investigations indicating the presence of Cu(I) in the MOF synthesized using different methods[32, 33]. We subsequently evaluated the porosity and Brunauer, Emmett and Teller (BET) areas using 77 K N_2 adsorption isotherms. A maximum BET area of 794 m^2 g^{-1} was calculated using Rouquerol's updated criteria implemented in BETSI (SI Fig. S4)[34]. This is the highest reported BET area for this material, comparable to the BET area of $Ni_3(HITP)_2$, and confirms permanent porosity, a key requirement for double-layer capacitance[27,35]. Elemental analysis confirmed that the as-synthesized $Cu_3(HHTP)_2$ has approximately the correct stoichiometric ratio of Cu and HHTP, although a small amount of a N-containing impurity was also present, most likely due to the use of ammonia as a modulator in the synthesis (see SI Methods).

Having characterized the crystalline structure and porosity of $Cu_3(HHTP)_2$, we next examined its electrical porosity of $Cu_3(HHTP)_2$, we next examined its electrical conductivity as this is a further key requirement for EDLC electrodes. The electrical conductivity of a pressed pellet of $Cu_3(HHTP)_2$ (two-point probe) was measured as 0.007 S cm^{-1} (see SI Methods). This is comparable to previously reported values for this MOF (0.0001 – 0.3 S cm^{-1} for polycrystalline samples)[21,28,31,36]. Composite films of $Cu_3(HHTP)_2$ (85 wt. % $Cu_3(HHTP)_2$, 10 wt. % carbon black, and 5 wt. % PTFE) of ca. 250 µm thickness were prepared by adapting the traditional literature method for the preparation of activated carbon (AC) films (see SI Methods)[37]. Carbon black was used as a conductive additive to increase the electrical conductivity of the film for use in EDLCs and has negligible contribution to the total capacitance of the cell (SI Fig. S5). Films made without the conductive additive (95 wt. % $Cu_3(HHTP)_2$ and 5 wt. % PTFE) displayed highly resistive behaviour in EDLCs and required very low current densities for analysis, showing the necessity of the conductive additive to achieve good capacitive performance (SI Figs. S6, S7). This indicates a limitation of using this MOF in EDLCs. Interestingly, Cu K-edge XANES on pristine film samples revealed evidence for the presence of Cu(I), with the amount of Cu(I) observed varying between samples (SI Fig. S8). Linear combination fitting of this XANES data with standard compounds indicated a maximal Cu(I) content of approximately 20 % (SI Fig. S9; Table S2). This underscores the sensitivity of $Cu_3(HHTP)_2$ and modification of the film-making procedure could be considered in future work if Cu(I) content proves to be problematic.

To investigate the electrochemical double-layer capacitance of $Cu_3(HHTP)_2$, symmetrical EDLCs were assembled using composite $Cu_3(HHTP)_2$ film electrodes and 1 M NEt_4BF_4 in acetonitrile electrolyte (see SI Methods). Cyclic voltammograms (CVs) and galvanostatic charge-discharge (GCD) experiments on these cells showed nearly rectangular and triangular traces respectively (**Fig. 2**), indicative of electrochemical double-layer capacitance. An initial cell voltage window of approximately 1.0 V, where primarily electric double-layer behaviour was observed, was established for $Cu_3(HHTP)_2$ by running CVs with progressively higher final voltages. Beyond 1.0 V, faradaic processes centered at ca. 1.1 V were observed (SI Fig. S10). This stable voltage window was confirmed by running CVs of $Cu_3(HHTP)_2$ composite electrodes in a three-electrode arrangement with 1 M NEt_4BF_4 in acetonitrile. Electric double-layer capacitive behaviour and no faradaic activity were observed for $Cu_3(HHTP)_2$ between the open circuit potential of +0.33 V and −0.27 V vs. Ag in the anodic direction, and between the open circuit potential of +0.19 V and +0.79 V vs. Ag in the cathodic direction (SI Figs. S11, S12). This is consistent with a working voltage window for $Cu_3(HHTP)_2$ EDLCs of approx. 1.0 – 1.2 V, which is further discussed below. This sharply contrasts to traditional activated carbons, which have a larger typical working voltage window of ca. 2.5 V with this electrolyte[38].

To evaluate and compare the capacitive performance of $Cu_3(HHTP)_2$ with other electrode materials, specific

capacitance (C_g) was calculated at a variety of current densities from GCD profiles using the *Supycap* Python code (see SI Methods). At a low current density of 0.04 – 0.05 A g^{-1}, the specific capacitance of $Cu_3(HHTP)_2$ in EDLCs as assembled above was recorded as 110 – 114 F g^{-1} when charged between 0 – 1 V (SI Fig. S13, Table S3). This value is very similar to that recorded previously for the almost isostructural framework $Ni_3(HITP)_2$ at a similar current density (111 – 116 F g^{-1}) in a similar EDLC with 1 M NEt_4BF_4 in acetonitrile[27]. Increasing the current density leads to a decrease in the specific capacitance (**Fig. 3**), again with very similar results to those reported for $Ni_3(HITP)_2$. Interestingly, these results suggest that the identity of the metal node (Cu or Ni) and ligating heteroatom (O or N) have little/no impact on the double-layer capacitance of these two frameworks. Indeed, $Ni_3(HITP)_2$ and $Cu_3(HHTP)_2$ have very similar 3D structures, with both formed from the eclipsed or near-eclipsed stacking of 2D π-d conjugated layers[18,31,39]. Therefore, our results suggest high capacitive performance arises from the three-dimensional structures of these MOFs. These results further suggest that the capacitance of an EDLC is uniquely defined by the 3D structure of the electrode and the electrolyte used. This generality has not been previously demonstrated using porous carbon materials, although further work is needed to confirm this hypothesis. The equivalent series resistances (*ESR*s) of the EDLC cells were measured using both electrochemical impedance spectroscopy (EIS) and GCD profiles, with *ESR*s of between 7 – 18 Ω obtained for a range of cells (SI Fig. S14).

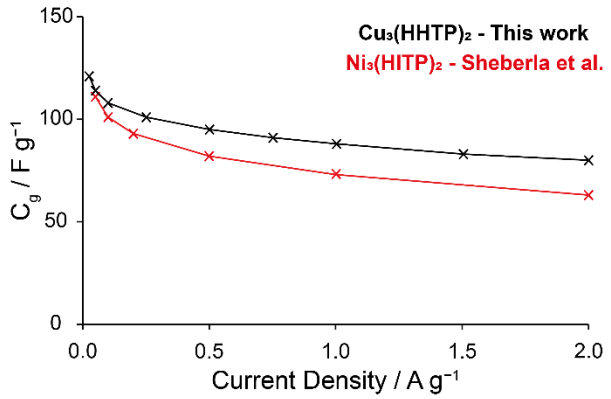

Figure 3: Comparison of specific capacitance versus current density graphs for $Cu_3(HHTP)_2$ and $Ni_3(HITP)_2$ (literature)[27]. This demonstrates the similarity in the capacitance of these MOFs in similar symmetric EDLCs.

Furthermore, we note higher capacitance retention (79 % between 0.25 – 2 A g^{-1}; 72 % between 0.25 – 2.5 A g^{-1}) than obtained in previous studies using $Cu_3(HHTP)_2$ powder electrodes in symmetric solid-state EDLCs (30 % up to 2 A g^{-1}), and capacitance retention on par with that obtained with $Cu_3(HHTP)_2$ NWAs in aqueous (58 % up to 2.5 A g^{-1}) and solid-state (60 % up to 2 A g^{-1}) EDLCs[28,29]. Although a direct comparison with solid-state cells is difficult due to the different phases of the electrolytes, these results illustrate that high capacitive behaviour can be achieved using $Cu_3(HHTP)_2$ powder and a conductive additive, which has a simpler synthesis than NWAs (SI Fig. S15). However, it must be noted that higher specific capacitances were observed for devices constructed with NWA electrodes (120 F g^{-1} at 0.5 A g^{-1} with a solid-state electrolyte; 195 F g^{-1} at 0.5 A g^{-1} with aqueous electrolyte) than observed in this work[28,29].

Another common metric used to compare EDLC performance of electrode materials is the areal (surface area normalized) capacitance. In this work, the areal capacitance of $Cu_3(HHTP)_2$ was calculated as approx. 14 μF cm^{-2} at 0.05 A g^{-1}. Although this is lower than that reported for $Ni_3(HITP)_2$ (18 μF cm^{-2}), significant variation in our values between 14 and 23 μF cm^{-2} was observed for EDLCs prepared using independent samples of $Cu_3(HHTP)_2$ with different BET surface areas (SI Table S4). We also observed variations in the performances of assembled EDLCs as a function of the areal mass loading of the electrodes. In general, EDLCs with higher areal mass loadings exhibited a more rapid decrease in capacitance as a function of current density and a higher ESR than those with lower areal mass loadings (SI Fig. S13, Table S3). This is consistent with previous observations but highlights the need for clear communication on mass loadings when comparing electrode performances[27,40].

To further investigate the suitability of $Cu_3(HHTP)_2$ for both practical supercapacitor applications and structure-property investigations, the voltage limits and cycling stability were studied in more detail. To probe the voltage limits of the cell, GCD experiments at a current density of 0.1 A g^{-1} were run with increasing final cell voltages from 0.6 V until the failure of the cell was observed. This showed an initial consistent increase in the specific capacitance with increasing final voltage followed by a rapid decrease upon cycling beyond 1.3 V (**Fig. 4a**). This demonstrates that the voltage limit of $Cu_3(HHTP)_2$ in a symmetric EDLC is approximately 1.3 V under these charging/discharging conditions, beyond which rapid degradation of the $Cu_3(HHTP)_2$ electrodes occurs causing irreversible loss in capacitance. Rapid capacitance loss when cycling above this cell voltage was confirmed via CV experiments cycling up to cell voltages of 1.6 V (SI Fig. S16). Degradation was confirmed by examining the Cu K-edge XANES of $Cu_3(HHTP)_2$ composite electrodes from an EDLC held at a cell voltage of 1.5 V for 1 h (SI Fig. S17). A shift of the absorption edge to a lower energy, in addition to the appearance of an inflection at ca. 8981 eV, indicate formation of Cu(I) in the negative electrode. In the positive electrode, the appearance of the feature at ca. 8981 eV indicates a significant change in the coordination environment around Cu to a lower symmetry environment. The shift of the rising edge to higher energies suggests an oxidation process may occur in the positive electrode too. These results indicate fundamental changes to the MOF structure in both electrodes and hint at potential degradation mechanisms, although further work is required to study these processes in more detail.

To further explore the working voltage window of $Cu_3(HHTP)_2$ EDLCs, Cu K-edge XANES studies were carried out on electrodes extracted from EDLCs held at different cell voltages for a period of 1 h (SI Fig. S18). For a cell voltage of 0.5 V, minimal changes were observed in the XANES

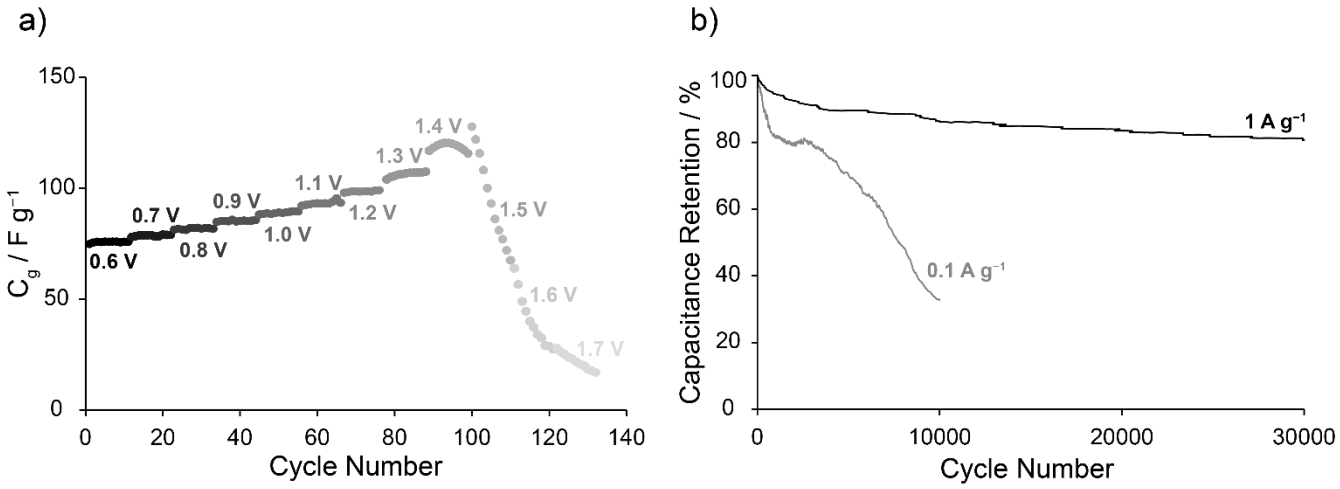

Figure 4: a) Specific capacitance, calculated from GCD profiles, against cycle number for increasing final cell voltages (see labels). This illustrates the voltage limit of the symmetric $Cu_3(HHTP)_2$ EDLC. b) Capacitance retention as a function of cycle number when cycling at 1 A g^{-1} and 0.1 A g^{-1} up to 1.0 V.

spectra. However, for a cell voltage of 0.8 V, the XANES data suggest structural changes to $Cu_3(HHTP)_2$ in the positive electrode. This suggests that kinetically slow faradaic processes may occur at cell voltages below 1.1 V but are missed due to the scan rates used in the above electrochemistry experiments (**Fig. 2**). This hypothesis was confirmed by obtaining a CV at a scan rate of 0.1 mV s^{-1} up to 1 V, with faradaic activity observed at this slow scan rate upon cycling past 0.8 V (SI Fig. S19). This highlights that $Cu_3(HHTP)_2$ may only be kinetically stable up to 1 V, a possible limitation that is explored further below.

Finally, the cycling stability of symmetric $Cu_3(HHTP)_2$ EDLCs was investigated at two different current densities in GCD experiments limited to a maximum cell voltage of 1 V. Reasonable cycling stability was observed when cycled between 0 – 1 V at 1 A g^{-1}, with capacitance retention of 81 % over 30,000 cycles (**Fig. 4b**). The capacitance retentions after 5,000 and 10,000 cycles (90 % and 86 %, respectively) compare well with the retentions of $Ni_3(HITP)_2$, approx. 90% over 10,000 cycles, and $Cu_3(HHTP)_2$ NWA devices with an aqueous electrolyte, 79.9 % over 5,000 cycles (SI Figs. S20, S21)[27,29]. This further highlights the similarities in electrochemical performance between $Ni_3(HITP)_2$ and $Cu_3(HHTP)_2$, and is further evidence that electrodes manufactured from $Cu_3(HHTP)_2$ powder can achieve high EDLC performance on par with those made with $Cu_3(HHTP)_2$ NWAs. Cu K-edge XANES showed minimal changes to the edge position and pre-edge peaks following this cycling, confirming the stability of $Cu_3(HHTP)_2$ upon extensive cycling at this current density (SI Fig. S22).

However, the capacitance retention of $Cu_3(HHTP)_2$ is significantly lower than that of YP50F, a commercial microporous AC, when cycled in an EDLC with 1 M NEt_4BF_4 in acetonitrile. In our work, YP50F exhibited a capacitance retention of 99 % over 10,000 cycles when cycled between 0 – 2.5 V at 2 A g^{-1} (SI Figs. S23, S24). This illustrates that, while this family of MOFs have specific and areal capacitances on par or exceeding current state-of-the-art carbons, significant improvement is required to achieve comparable cycling stability. This is the first work to call attention to this key difference and illustrates a major disadvantage of using this family of conductive MOFs in EDLCs instead of ACs, as high cycling stability is a crucial property of an EDLC. Furthermore, the capacitance retention of $Cu_3(HHTP)_2$ EDLCs in this work was significantly lower when cycled at a lower current density of 0.1 A g^{-1}, with only 32 % capacitance retention after 10,000 cycles (**Fig. 4b**). An increase in the intensity of the pre-edge feature at ca. 8981 eV was observed in the Cu K-edge XANES of the positive electrode following cycling, again indicative of a change in the MOF structure. A shift in the absorption edge energy to a lower value was also seen, hinting at possible Cu(I) formation. This confirms degradation at this current density (SI Fig. S25) and further emphasizes that $Cu_3(HHTP)_2$ is only kinetically stable when cycled between 0 – 1 V. This is also the first work to highlight the difference in capacitance retention at different current densities with this family of conducting frameworks. These findings raise questions about the practical applicability of these frameworks in commercial devices. Future studies to identify the degradation mechanisms in these frameworks may allow for the design of conductive MOFs with wider double-layer stability windows, and thus improved capacitive performances. Given the observation of redox processes centered on the Cu nodes by XANES, varying the metal node or organic linker molecule may be a viable method to increase the potential window[41].

Conclusion

We have demonstrated that the conductive MOF $Cu_3(HHTP)_2$ displays good capacitive behaviour in symmetric EDLCs with 1 M NEt_4BF_4 in acetonitrile, with a specific capacitance of 110 – 114 F g^{-1} at 0.04 – 0.05 A g^{-1} recorded. Our work shows that the previously observed capacitive behaviour of $Ni_3(HITP)_2$ is not unique amongst layered conducting MOFs and has expanded the family of conductive MOFs which is known to display capacitive

performance in EDLCs with organic electrolytes. Notably, $Cu_3(HHTP)_2$ can be synthesized using all commercially available starting materials, and we have demonstrated that standard electrode fabrication techniques using $Cu_3(HHTP)_2$ powder can be employed with this framework to achieve good capacitive performance, making this framework an accessible model system for further study. However, our work also illustrates several limitations of using current conductive MOFs in EDLCs, notably the significantly lower cycling stability and stable double-layer voltage window relative to state-of-the-art carbon materials. This raises questions about the practical applicability of these frameworks in commercial devices. Despite this, the similarity in the specific capacitances of $Cu_3(HHTP)_2$ and $Ni_3(HITP)_2$ at low current densities with the same organic electrolyte shows that the capacitive performance is independent of the identity of the metal node and organic linker molecule for these two frameworks. Importantly, this suggests that the capacitive performance of an EDLC more generally is uniquely defined by the 3D structure of the electrodes and the electrolyte, although further work is required to test this significant hypothesis.

Experimental Section

Synthesis of $Cu_3(HHTP)_2$. $Cu_3(HHTP)_2$ was synthesized by modifying a recently published literature procedure[30]. A solution of $Cu(NO_3)_2.3H_2O$ (0.127 g, 0.526 mmol, 1.65 eq) and aqueous ammonia (35 %) solution (0.829 mL, 15.0 mmol, 47 eq) in distilled water (2 mL) was prepared. The resulting dark blue solution was added dropwise to a dispersion of 2,3,6,7,10,11-hexahydroxytriphenylene hydrate, $H_6HHTP.xH_2O$, (0.103 g, 0.318 mmol, 1.00 eq) in distilled water (8.4 mL). The resulting mixture was heated in a furnace oven in a 40 mL screw vial (Thermo Scientific; B7999-6), closed with a screw cap fitted with a septum as a safety precaution in the event of over pressurization, at 80 °C for 24 h. The dark blue precipitate formed was separated by centrifugation, and the supernatant layer was discarded. The dark blue precipitate was then washed successively with water (3 × 30 mL), ethanol (4 × 30 mL), and acetone (4 × 30 mL). Washing was performed by centrifuging the precipitate with the desired washing solvent for 15 – 30 minutes before removing the supernatant layer and replacing with fresh washing solvent. No soaking of the precipitate was performed. The resulting dark blue powder was dried at 75 °C under dynamic vacuum for 72 h and then stored in a N_2-filled glovebox until used.

We found that rapid washing (completed in ca. 5 h) and activation of the synthesized $Cu_3(HHTP)_2$ to minimize its exposure to air was required to ensure a high porosity and a wider stable double-layer voltage window.

Elemental Analysis. Laboratory elemental analysis was performed on $Cu_3(HHTP)_2$ as synthesized above.

Cu content was determined via inductively coupled plasma optical emission spectroscopy (ICP-OES) using a Thermo Scientific iCAP-7400 ICP spectrometer. 1.3610 mg of $Cu_3(HHTP)_2$ was digested in 5 mL of concentrated HNO_3 (67 – 69 %, trace metal, Fisher Scientific), and the sample diluted with 5 mL of water. A 0.5 mL aliquot was then diluted to 10 mL with water. Cu concentration of the resulting solution was determined using calibration curves constructed from standard solutions (Multi-element standard solution for ICP IV, Fisher Scientific). C, H and N content was determined via CHN combustion analysis using an Exeter Analytical CE-440, with combustion at 975 °C.

Calculated for $Cu_3(HHTP)_2$: Cu, 23.1 wt. %; C, 52.3 wt. %; H, 1.5 wt. %.

Experimental results for $Cu_3(HHTP)_2$ synthesized above: Cu, 21.7 wt. %; C, 48.9 wt. %; H, 2.4 wt. %; N, 2.8 wt. %.

These results confirm that the as-synthesized $Cu_3(HHTP)_2$ has approximately the correct stoichiometric ratio of Cu and HHTP. It also indicates the potential presence of a N-containing impurity leftover in the MOF following washing.

X-ray Diffraction. Laboratory powder X-ray diffraction data were collected on a Malvern Panalytical Empyrean instrument, equipped with an X'celerator Scientific detector using non-monochromated Cu K_α radiation (λ = 1.5418 Å). Borosilicate glass capillary tubes (0.5 mm outside diameter, 0.01 mm wall thickness; Capillary Tube Supplies Ltd.) were loaded with the sample in a N_2-filled glovebox, with NiCr wire used to aid packing. The capillary was then sealed in the N_2-filled glovebox using EA 3430 epoxy adhesive (Loctite), which was allowed to cure for 5 h before removing the capillary from the glovebox. The data were collected at room temperature over a 2θ range of 3 – 50 °, with an effective step size of 0.017 ° and a total collection time per scan of 1 h. Multiple scans were chosen to minimize the possibility of saturating the detector as well as to detect any possible changes with time (none were observed). The presented experimental PXRD is a sum average of 15 scans.

Simulated PXRD patterns were produced using GSAS-II Crystallography Data Analysis Software[42]. Computational structures used to produce the simulated PXRD patterns and XANES are available at: https://doi.org/10.5281/zenodo.4694845

Gas Adsorption Measurements. Low pressure N_2 isotherms (adsorption and desorption) were collected using a Micromeritics 3Flex at 77 K. Prior to analysis, samples were degassed in a Schlenk flask at 80 °C for 24 h. In-situ degassing (80 °C, 24 h) was further performed on a Micromeritics VacPrep. Material BET areas were calculated from the isotherms using the BET equation and Rouquerol's consistency criteria implemented in BETSI[32, 43]. The micropore volume (W_o) and the total (V_{tot}) pore volumes were calculated at P/P_o of 0.1 and 0.99, respectively. For $Cu_3(HHTP)_2$, a Type I N_2 isotherm was observed, with high gas uptake below 0.1 P/P_o indicating extensive microporosity. See the Appendix for full BETSI readouts.

Conductivity Measurements. The electrical conductivity of $Cu_3(HHTP)_2$ samples was measured via a two-point probe method using a homemade set-up. Samples were pressed between two stainless steel electrodes using a hydraulic press (Specac). Insulating PTFE disks were used to prevent a short circuit through the press. All measurements were conducted with a loading of between 1.50 – 1.57 ton-force cm^{-2}. Resistances were measured using a Keithley 2000 Multimeter.

The conductivity, σ (S cm^{-1}), of the sample was calculated according to: $\sigma = L / RA$, where L is the thickness of the sample (cm), A is the area of the sample (cm^2), and R is the measured resistance (Ω). All values of L and A were measured following completion of the measurement, assuming a non-elastic material. Based on multiple measurements of the resistance and the thickness of the sample, the error on the calculated conductivity value is ca. ± 6.6 %.

Pellets composed of $Cu_3(HHTP)_2$ were prepared by loading the material into a 13 mm Evacuable Pellet Die (Specac) and applying a force of 3 ton-force cm^{-2} for 5 mins with a hydraulic press (Specac). The areal mass loading of the pellets was approximately 50 mg cm^{-2}. The thickness of the pellets was measured using a digital micrometer (Mitutoyo) as approximately 330 μm.

Electrode Film Preparation. Freestanding composite MOF films were prepared by adapting the traditional literature method for activated carbons[11]. $Cu_3(HHTP)_2$ powder and acetylene black were lightly ground together in a vial before ethanol (ca. 1.5 mL) was added to produce a loose slurry. This was sonicated for 15 mins before being added to PTFE dispersion (60 wt. % in water) in a few drops of ethanol in a watchglass. The slurry was stirred by hand in the watchglass for 40 mins in ambient conditions. The film was gradually formed upon drying of the slurry before being transferred to a glass surface, where it was kneaded for 20 mins to ensure homogenous incorporation of the active materials and PTFE and then rolled into a freestanding film using a homemade aluminum rolling pin. The film was dried in vacuo at 75 °C for at least 48 h to remove any remaining ethanol. The masses of components were calculated so that the final film had a composition of 85 wt. % $Cu_3(HHTP)_2$, 10 wt. % acetylene black, and 5 wt. % PTFE.

Freestanding acetylene black, YP50F, and $Cu_3(HHTP)_2$ films were prepared using the same technique. These had a final composition of 95 wt. % electroactive material and 5 wt. % PTFE.

EDLC Assembly. Symmetric electric double-layer capacitors (EDLCs) with $Cu_3(HHTP)_2$ composite and acetylene black film electrodes were prepared in Swagelok PFA-820-6 union tube fittings with homemade stainless-steel plugs as current collectors. Electrodes were cut from freestanding films in a N_2-filled glovebox using a ¼'' stainless steel manual punching cutter (Hilka Tools), with areal mass loadings ranging between 10 – 35 mg cm^{-2}. An excess of 1 M tetraethylammonium tetrafluoroborate (NEt_4BF_4) in anhydrous acetonitrile was used as an electrolyte. This solution was prepared in a N_2-filled glovebox. Whatman glass microfiber filter (GF/A), cut with a ⅜'' stainless steel manual punching cutter, was used as separator. This was dried in vacuo at 100 °C for 24 h prior to use. EDLCs were hand-sealed until air-tight before being removed from the glovebox for electrochemical testing.

Symmetric electric double-layer capacitors (EDLCs) with YP50F film electrodes were prepared as coin cells in CR2032 SS316 coin cell cases (Cambridge Energy Solutions). Electrodes were cut from freestanding YP50F films with areal mass loadings ranging between 10 – 15 mg cm^{-2}. The electrodes were dried in vacuo at 100 °C for at least 24 h prior to assembling the cell in a N_2-filled glovebox. A 1 M solution of NEt_4BF_4 in anhydrous acetonitrile was used as an electrolyte. This solution was prepared in a N_2-filled glovebox. Whatman glass microfiber filter (GF/A) was used as separator. This was dried in vacuo at 100 °C for 24 h prior to use. Each coin cell contained two SS316 separator disks and one SS316 spring to ensure sufficient pressure in the cell. The coin cells were sealed in the glovebox using a Compact Hydraulic Coin Cell Crimper (Cambridge Energy Solutions).

$Cu_3(HHTP)_2$ composite cells were assembled in Swagelok PFA-820-6 union tube fittings as opposed to in CR2032 SS316 coin cell cases (Cambridge Energy Solutions) as the removal of the electrodes for subsequent analysis without discharging the cell was easier from the fittings.

Three-Electrode Cell Assembly. Three-electrode cells were prepared in Swagelok PFA-820-3 union tube fittings with homemade stainless-steel plugs as current collectors. $Cu_3(HHTP)_2$ composite electrodes with areal mass loadings ranging between 12 – 20 mg cm^{-2} were used as working electrodes. Overcapacitive YP50F activated carbon film electrodes with areal mass loadings of 35 – 40 mg cm^{-2} were used as counter electrodes. Ag wire was used as a pseudo-reference electrode. A 1 M solution of tetraethylammonium tetrafluoroborate (NEt_4BF_4) in anhydrous acetonitrile was used as an electrolyte. All measurements were performed under dry and oxygen-free conditions in a N_2-filled glove box. Under these conditions, the ferrocene–ferricenium (Fc/Fc^+) redox couple was measured at 0.63 ± 0.01 V versus Ag. All potentials discussed for the three-electrode cell are referenced to Ag.

Electrochemical Characterization. All electrochemical measurements were carried out using Biologic SP-150 and VSP-3e potentiostats and a Biologic BCS-800 Series ultra-precision battery cycler. Electrochemical Impedance Spectroscopy (EIS) measurements were performed in the frequency range from 200 kHz to 3 – 10 mHz using a single-sinusoidal signal with a sinus amplitude of 10 mV. No drift correction was applied. The specific capacitance, C_g (F g^{-1}), was calculated from galvanostatic charge-discharge (GCD) discharge profiles using the *Supycap* Python code. C_g values were determined using only the mass of active material (i.e., Cu_3HHTP_2) in the EDLCs.

The equivalent series resistance (ESR) was calculated from both Nyquist plots (produced from EIS measurements) and from the voltage drop at the beginning of GCD discharge profiles. For the calculation from Nyquist plots, the ESR was obtained from extrapolation of the low frequency response onto the real (Re(Z)) axis, as is consistent with the literature[44]. For the calculation from GCD discharge profiles, the *Supycap* Python code was used.

Current densities were calculated by dividing the current applied during the GCD experiment, I, by the average mass of active material per electrode, $\bar{m}$.

For full details of the calculations and methods used in the *Supycap* Python code, please visit: GitHub - AdaYuanChen/Supycap: Analysis tool for the CC and CV experiment of supercapacitors

X-ray Absorption Spectroscopy. Cu K-edge X-ray absorption near edge structure (XANES) measurements were performed at the B18 beamline at Diamond Light Source. Measurements at the Cu K-edge were recorded in fluorescence yield mode. Energy calibration was done with Cu metal as a reference. XANES data were processed and analyzed using the Athena program of the Demeter software package[45].

XANES electrode samples were prepared from the disassembly of EDLC cells. The cells were disassembled in a N_2-filled glovebox and the electrodes were isolated and packaged into air-tight foil/poly pouches (Sigma-Aldrich). Cu(I) standard samples (Cu_2O, CuOAc) were prepared by grinding a small amount (ca. 5 wt. %) of the standard with cellulose in a N_2-filled glovebox before packaging into an air-tight foil/poly pouch. Cu(II) standard samples (CuO, $Cu(OAc)_2$) were prepared by grinding a small amount of the standard (ca. 5 wt. %) with cellulose in ambient conditions before pressing into a pellet using a hydraulic press (Specac) as described previously.

In this work, the edge is defined as the energy at normalized $x\mu(E)$ = 0.5.

XANES calculations were done using the FEFF 9.0 code[46, 47]. The Full Multiple Scattering (*FMS*) and Self Consistent Field (*SCF*) radii were set to 8.0 Å and 7.5 Å respectively and calculations were done using the Hedin-Lundqvist exchange correlation potential. The exchange potential was offset by 2 eV to account for errors in the calculated Fermi level, and 0.5 eV imaginary energy was added to correct for instrumental broadening. All other FEFF parameters were set to the default values. A red shift of the simulated spectra was required to align it with the experimental spectrum.

ASSOCIATED CONTENT

Supporting Information

The Supplementary Information (SI) is available free of charge on the ACS Publications website.

Details of materials used, PXRD analysis, gas sorption analysis, additional electrochemistry data and analysis, and additional XANES data and analysis (PDF).

AUTHOR INFORMATION

Corresponding Author

* acf50@cam.ac.uk (A.C.F.)

Notes

The authors declare no competing financial interests.

ACKNOWLEDGMENT

J.W.G. acknowledges the School of the Physical Sciences (Cambridge) for the award of an Oppenheimer Studentship. This work was supported by the Faraday Institution [grant number FIRG017], via a Faraday Undergraduate Summer Experience (FUSE) internship to Y.C. The work at Imperial (A.W.) was supported by a Royal Society University Research Fellowship (UF100278) and benefited from the UK Materials and Molecular Modelling Hub for computational resources, which is partially funded by EPSRC (EP/P020194/1 and EP/T022213/1). M.J.G. thanks the Royal Society for PhD funding. D.F.-J. thanks the European Research Council (ERC) under the European Union's Horizon 2020 Research and Innovation Programme (NanoMOFdeli), ERC-2016-COG 726380, and Innovate UK (104384). S.E.D. acknowledges funding from the Winton Programme for the Physics of Sustainability (Cambridge). A.C.F. thanks the Isaac Newton Trust of Trinity College (Cambridge) for a Research Grant (G101121), and the Department of Chemistry (Cambridge) for the award of a BP Next Generation Fellowship. This work was also supported by a UKRI Future Leaders Fellowship to A.C.F. (MR/T043024/1). We thank the Diamond Light Source for the award of beam time as part of the Energy Materials Block Allocation Group SP14239. We thank Dr. Phillip Milner and Dr. Lewis Owen for collaboration and stimulating discussion over the course of the project. We thank Dr. Chris Truscott and Dr. Nigel Howard for collaboration and technical expertise.

REFERENCES

(1) World Energy Outlook 2019. *World Energy Outlook; OECD* **2019**. https://doi.org/10.1787/caf32f3b-en.

(2) al Shaqsi, A. Z.; Sopian, K.; Al-Hinai, A. Review of Energy Storage Services, Applications, Limitations, and Benefits. *Energy Reports* **2020**, 288–306.

(3) Gü, T. M. Review of Electrical Energy Storage Technologies, Materials and Systems: Challenges and Prospects for Large-Scale Grid Storage. *Energy & Environmental Science* **2018**, *11*, 2696.

(4) González, A.; Goikolea, E.; Barrena, J. A.; Mysyk, R. Review on Supercapacitors: Technologies and Materials. *Renewable and Sustainable Energy Reviews* **2016**, 1189–1206.

(5) Simon, P.; Gogotsi, Y.; Dunn, B. Where Do Batteries End and Supercapacitors Begin? *Science* **2014**, *343* (6176), 1210–1211.

(6) Liu, X.; Li, K. Energy Storage Devices in Electrified Railway Systems: A Review. *Transportation Safety and Environment* **2020**, *2* (3), 183–201.

(7) Miller, E. E.; Hua, Y.; Tezel, F. H. Materials for Energy Storage: Review of Electrode Materials and Methods of Increasing Capacitance for Supercapacitors. *Journal of Energy Storage* **2018**, 30–40.

(8) Méndez-Morales, T.; Ganfoud, N.; Li, Z.; Haefele, M.; Rotenberg, B.; Salanne, M. Performance of Microporous Carbon Electrodes for Supercapacitors: Comparing Graphene with Disordered Materials. *Energy Storage Materials* **2019**, *17*, 88–92.

(9) Chmiola, J.; Yushin, G.; Dash, R.; Gogotsi, Y. Effect of Pore Size and Surface Area of Carbide Derived Carbons on Specific Capacitance. *Journal of Power Sources* **2006**, *158* (1), 765–772.

(10) Largeot, C.; Portet, C.; Chmiola, J.; Taberna, P. L.; Gogotsi, Y.; Simon, P. Relation between the Ion Size and Pore Size for an Electric Double-Layer Capacitor. *Journal of the American Chemical Society* **2008**, *130* (9), 2730–2731.

(11) Chmiola, J.; Yushin, G.; Gogotsi, Y.; Portet, C.; Simon, P.; Taberna, P. L. Anomalous Increase in Carbon at Pore Sizes Less than 1 Nanometer. *Science* **2006**, *313* (5794), 1760–1763.

(12) Centeno, T. A.; Sereda, O.; Stoeckli, F. Capacitance in Carbon Pores of 0.7 to 15 Nm: A Regular Pattern. *Physical Chemistry Chemical Physics* **2011**, *13* (27), 12403–12406.

(13) Stoeckli, F.; Centeno, T. A. Optimization of the Characterization of Porous Carbons for Supercapacitors. *Journal of Materials Chemistry A* **2013**, *1*, 6865–6873.

(14) Raymundo-Piñero, E.; Kierzek, K.; Machnikowski, J.; Béguin, F. Relationship between the Nanoporous Texture of Activated Carbons and Their Capacitance Properties in Different Electrolytes. *Carbon* **2006**, *44* (12), 2498–2507.

(15) Liu, J.; Song, X.; Zhang, T.; Liu, S.; Wen, H.; Chen, L. 2D Conductive Metal–Organic Frameworks: An Emerging Platform for Electrochemical Energy Storage. *Angewandte Chemie - International Edition* **2020**. https://doi.org/10.1002/anie.202006102.

(16) Xie, L. S.; Skorupskii, G.; Dincă, M. Electrically Conductive Metal-Organic Frameworks. *Chemical Reviews* **2020**, 8536–8580.

(17) Hmadeh, M.; Lu, Z.; Liu, Z.; Gándara, F.; Furukawa, H.; Wan, S.; Augustyn, V.; Chang, R.; Liao, L.; Zhou, F.; Perre, E.; Ozolins, V.; Suenaga, K.; Duan, X.; Dunn, B.; Yamamto, Y.; Terasaki, O.; Yaghi, O. M. New Porous Crystals of Extended Metal-Catecholates. *Chemistry of Materials* **2012**, *24* (18), 3511–3513.

(18) Ko, M.; Mendecki, L.; Mirica, K. A. Conductive Two-Dimensional Metal-Organic Frameworks as Multifunctional Materials. *Chemical Communications* **2018**, *54*, 7873.

(19) Sun, L.; Campbell, M. G.; Dincə, M. Electrically Conductive Porous Metal-Organic Frameworks. *Angewandte Chemie - International Edition* **2016**, 3566–3579.

(20) Dou, J.-H.; Arguilla, M. Q.; Luo, Y.; Li, J.; Zhang, W.; Sun, L.; Mancuso, J. L.; Yang, L.; Chen, T.; Parent, L. R.; Skorupskii, G.; Libretto, N. J.; Sun, C.; Yang, M. C.; Dip, P. V.; Brignole, E. J.; Miller, J. T.; Kong, J.; Hendon, C. H.; Sun, J.; Dincă, M. Atomically Precise Single-Crystal Structures of Electrically Conducting 2D Metal–Organic Frameworks. *Nature Materials* **2021**, *20*, 222–228.

(21) Nam, K. W.; Park, S. S.; dos Reis, R.; Dravid, V. P.; Kim, H.; Mirkin, C. A.; Stoddart, J. F. Conductive 2D Metal-Organic Framework for High-Performance Cathodes in Aqueous Rechargeable Zinc Batteries. *Nature Communications* **2019**, *10* (1).

(22) Feng, D.; Lei, T.; Lukatskaya, M. R.; Park, J.; Huang, Z.; Lee, M.; Shaw, L.; Chen, S.; Yakovenko, A. A.; Kulkarni, A.; Xiao, J.; Fredrickson, K.; Tok, J. B.; Zou, X.; Cui, Y.; Bao, Z. Robust and Conductive Two-Dimensional Metal– Organic Frameworks with Exceptionally High Volumetric and Areal Capacitance. *Nature Energy* **2018**, *3*, 30–36.

(23) Gu, S.; Bai, Z.; Majumder, S.; Huang, B.; Chen, G. Conductive Metal–Organic Framework with Redox Metal Center as Cathode for High Rate Performance Lithium Ion Battery. *Journal of Power Sources* **2019**, *429*, 22–29.

(24) Cai, D.; Lu, M.; Li, L.; Cao, J.; Chen, D.; Tu, H.; Li, J.; Han, W. A Highly Conductive MOF of Graphene Analogue Ni3(HITP)2 as a Sulfur Host for High-Performance Lithium–Sulfur Batteries. *Small* **2019**, *15* (44).

(25) Li, F.; Zhang, X.; Liu, X.; Zhao, M. Novel Conductive Metal-Organic Framework for a High-Performance Lithium-Sulfur

Battery Host: 2D Cu-Benzenehexathial (BHT). *ACS Applied Materials and Interfaces* **2018**, *10* (17), 15012–15020.

(26) Dong, S.; Wu, L.; Xue, M.; Li, Z.; Xiao, D.; Xu, C.; Shen, L.; Zhang, X. Conductive Metal–Organic Framework for High Energy Sodium-Ion Hybrid Capacitors. *ACS Applied Energy Materials* **2021**, *4* (2), 1568–1574.

(27) Sheberla, D.; Bachman, J. C.; Elias, J. S.; Sun, C. J.; Shao-Horn, Y.; Dincă, M. Conductive MOF Electrodes for Stable Supercapacitors with High Areal Capacitance. *Nature Materials* **2017**, *16* (2), 220–224.

(28) Li, W. H.; Ding, K.; Tian, H. R.; Yao, M. S.; Nath, B.; Deng, W. H.; Wang, Y.; Xu, G. Conductive Metal–Organic Framework Nanowire Array Electrodes for High-Performance Solid-State Supercapacitors. *Advanced Functional Materials* **2017**, *27* (27).

(29) Du, X.; Zhang, J.; Wang, H.; Huang, Z.; Guo, A.; Zhao, L.; Niu, Y.; Li, X.; Wu, B.; Liu, Y. Solid-Solid Interface Growth of Conductive Metal-Organic Framework Nanowire Arrays and Their Supercapacitor Application. *Materials Chemistry Frontiers* **2020**, *4* (1), 243–251.

(30) Hoppe, B.; Hindricks, K. D. J.; Warwas, D. P.; Schulze, H. A.; Mohmeyer, A.; Pinkvos, T. J.; Zailskas, S.; Krey, M. R.; Belke, C.; König, S.; Fröba, M.; Haug, R. J.; Behrens, P. Graphene-like Metal-Organic Frameworks: Morphology Control, Optimization of Thin Film Electrical Conductivity and Fast Sensing Applications. *CrystEngComm* **2018**, *20* (41), 6458–6471.

(31) Day, R. W.; Bediako, D. K.; Rezaee, M.; Parent, L. R.; Skorupskii, G.; Arguilla, M. Q.; Hendon, C. H.; Stassen, I.; Gianneschi, N. C.; Kim, P.; Dincă, M. Single Crystals of Electrically Conductive Two-Dimensional Metal-Organic Frameworks: Structural and Electrical Transport Properties. *ACS Central Science* **2019**, *5* (12), 1959–1964.

(32) Misumi, Y.; Yamaguchi, A.; Zhang, Z.; Matsushita, T.; Wada, N.; Tsuchiizu, M.; Awaga, K. Quantum Spin Liquid State in a Two-Dimensional Semiconductive Metal-Organic Framework. *Journal of the American Chemical Society* **2020**, *142* (39), 16513–16517.

(33) Mendecki, L.; Mirica, K. A. Conductive Metal-Organic Frameworks as Ion-to-Electron Transducers in Potentiometric Sensors. *ACS Applied Materials and Interfaces* **2018**, *10* (22), 19248–19257.

(34) Osterrieth, J. W. M.; Rampersad, J.; Madden, D.; Rampal, N.; Skoric, L.; Connolly, B.; Allendorf, M. D.; Stavila, V.; Snider, J. L.; Ameloot, R.; Marreiros, J.; Ania, C.; Azevedo, D.; Vilarrasa-Garcia, E.; Santos, B. F.; Bu, X.-H.; Zang, X.; Bunzen, H.; Champness, N. R.; Griffin, S. L.; Chen, B.; Lin, R.-B.; Coasne, B.; Cohen, S.; Moreton, J. C.; Colon, Y. J.; Chen, L.; Clowes, R.; Coudert, F.-X.; Cui, Y.; Hou, B.; D, D. M.; Doheny, P. W.; Dincă, M.; Sun, C.; Doonan, C.; Thomas Huxley, M.; Evans, J. D.; Falcaro, P.; Ricco, R.; Farha, O.; Idrees, K. B.; Islamoglu, T.; Feng, P.; Yang, H.; Forgan, R. S.; Bara, D.; Furukawa, S.; Sanchez, E.; Gascon, J.; Telalovic, S.; Ghosh, S. K.; Mukherjee, S.; Hill, M. R.; Munir Sadiq, M.; Horcajada, P.; Salcedo-Abraira, P.; Kaneko, K.; Kukobat, R.; Kenvin, J.; Keskin, S.; Kitagawa, S.; Otake, K.; Lively, R. P.; A DeWitt, S. J.; Llewellyn, P.; Lotsch, B. v; Emmerling, S. T.; Pütz, A. M.; Martí-Gastaldo, C.; Padial, N. M.; García-Martínez, J.; Linares, N.; Maspoch, D.; Suárez del Pino, J. A.; Moghadam, P.; Oktavian, R.; Morris, R. E.; Wheatley, P. S.; Navarro, J.; Petit, C.; Danaci, D.; Rosseinsky, M. J.; Katsoulidis, A. P.; Schröder, M.; Han, X.; Yang, S.; van der Veen, M. A.; Rega, D.; van Speybroeck, V.; J Rogge, S. M.; Lamaire, A.; Walton, K. S.; Bingel, L. W.; Wuttke, S.; Andreo, J.; Yaghi, O.; Zhang, B.; Yavuz, C. T.; Nguyen, T. S.; Zamora, F.; Montoro, C.; Zhou, H.; Kirchon, A.; Fairen-Jimenez, D. How Reproducible Are Surface Areas Calculated from the BET Equation? *ChemRxiv [Preprint]* **2021**. https://doi.org/10.26434/chemrxiv.14291644.v1

(35) Bi, S.; Banda, H.; Chen, M.; Niu, L.; Chen, M.; Wu, T.; Wang, J.; Wang, R.; Feng, J.; Chen, T.; Dincă, M.; Kornyshev, A. A.; Feng, G. Molecular Understanding of Charge Storage and Charging Dynamics in Supercapacitors with MOF Electrodes and Ionic Liquid Electrolytes. *Nature Materials* **2020**, *19* (5), 552–558.

(36) Rubio-Giménez, V.; Galbiati, M.; Castells-Gil, J.; Almora-Barrios, N.; Navarro-Sánchez, J.; Escorcia-Ariza, G.; Mattera, M.; Arnold, T.; Rawle, J.; Tatay, S.; Coronado, E.; Martí-Gastaldo, C. Bottom-Up Fabrication of Semiconductive Metal–Organic Framework Ultrathin Films. *Advanced Materials* **2018**, *30* (10).

(37) Dyatkin, B.; Presser, V.; Heon, M.; Lukatskaya, M. R.; Beidaghi, M.; Gogotsi, Y. Development of a Green Supercapacitor Composed Entirely of Environmentally Friendly Materials. *ChemSusChem* **2013**, *6* (12), 2269–2280.

(38) Eguchi, T.; Tashima, D.; Fukuma, M.; Kumagai, S. Activated Carbon Derived from Japanese Distilled Liquor Waste: Application as the Electrode Active Material of Electric Double-Layer Capacitors. *Journal of Cleaner Production* **2020**, *259*.

(39) Chen, T.; Dou, J. H.; Yang, L.; Sun, C.; Libretto, N. J.; Skorupskii, G.; Miller, J. T.; Dincă, M. Continuous Electrical Conductivity Variation in M3(Hexaiminotriphenylene)2(M = Co, Ni, Cu) MOF Alloys. *Journal of the American Chemical Society* **2020**, *142* (28), 12367–12373.

(40) Bhattacharjya, D.; Carriazo, D.; Ajuria, J.; Villaverde, A. Study of Electrode Processing and Cell Assembly for the Optimized Performance of Supercapacitor in Pouch Cell Configuration. *Journal of Power Sources* **2019**, *439*, 227106.

(41) Iqbal, R.; Sultan, M. Q.; Hussain, S.; Hamza, M.; Tariq, A.; Akbar, M. B.; Ma, Y.; Zhi, L. The Different Roles of Cobalt and Manganese in Metal-Organic Frameworks for Supercapacitors. *Advanced Materials Technologies* **2021**, 2000941.

(42) Toby, B. H.; von Dreele, R. B. GSAS-II: The Genesis of a Modern Open-Source All Purpose Crystallography Software Package. *Journal of Applied Crystallography* **2013**, *46* (2), 544–549.

(43) Gómez-Gualdrón, D. A.; Moghadam, P. Z.; Hupp, J. T.; Farha, O. K.; Snurr, R. Q. Application of Consistency Criteria to Calculate BET Areas of Micro- and Mesoporous Metal-Organic Frameworks. *Journal of the American Chemical Society* **2016**, *138* (1), 215–224.

(44) Vicentini, R.; da Silva, L. M.; Cecilio, E. P.; Alves, T. A.; Nunes, W. G.; Zanin, H. How to Measure and Calculate Equivalent Series Resistance of Electric Double-Layer Capacitors. *Molecules* **2019**, *24* (8).

(45) Ravel, B.; Newville, M. ATHENA, ARTEMIS, HEPHAESTUS: Data Analysis for X-Ray Absorption Spectroscopy Using IFEFFIT. *Journal of Synchrotron Radiation* **2005**, *12*, 537–541.

(46) Rehr, J. J.; Kas, J. J.; Vila, F. D.; Prange, M. P.; Jorissen, K. Parameter-Free Calculations of X-Ray Spectra with FEFF9. *Physical Chemistry Chemical Physics* **2010**, *12*, 5503–5513.

(47) Rehr, J. J.; Kas, J. J.; Prange, M. P.; Sorini, A. P.; Takimoto, Y.; Vila, F. Ab Initio Theory and Calculations of X-Ray Spectra. *Comptes Rendus Physique*. **2009**, *10* (6), 548–559.

Table of Contents Image